A benchmark of industrial polymerization process for thermal runaway process monitoring

Highlights

A benchmark of industrial polymerization process for thermal runaway process monitoring

Simin Li, Shuang-hua Yang, Yi Cao, Xiaoping Jiang, Chenchen Zhou

- Clarify the need for polymerization benchmark study to develop monitoring algorithms;
- The first publicly available dynamic model for a simplified industrial polymerization process;
- Extract and simulate five types of faults that could lead to thermal runaway;
- Two types of monitoring algorithms tested on the dataset show the applicability and suitability of the benchmark model.

A benchmark of industrial polymerization process for thermal runaway process monitoring

Simin Li[a], Shuang-hua Yang[a,b,c,*], Yi Cao[a,b], Xiaoping Jiang[d], Chenchen Zhou[a,b]

[a]*Zhejiang University, No.866 Yuhangtang Road, Hangzhou, 310030, Zhejiang, China*
[b]*Institute of Zhejiang University-Quzhou, No.78 Jiuhua North Avenue, Quzhou, 324003, Zhejiang, China*
[c]*University of Reading, Whiteknights Campus, Reading, RG6 6UR, Berkshire, United Kingdom*
[d]*Ningbo Tech University, No.1 South Qianhu Road, Ningbo, 315100, Zhejiang, China*

Abstract

Polymer production is of paramount importance in the chemical manufacturing industry. However, safety concerns are prevalent due to the exothermic nature of polymerization reactions, which can cause thermal runaway. The limitations of the current industry-standard monitoring methods underscore the need for novel techniques to detect faults early. To facilitate the development and evaluation of such algorithms, benchmarks that enable direct comparisons of performance are required. Addressing this gap, the present work first introduces an open-source polymerization benchmark model and associated datasets. Derived from reaction kinetics, mass balance, and energy balance analysis, the differential equation forms the basis of our model. By manipulating relative parameters, we intentionally induce five typical faults that can lead to thermal runaway. As a result, our benchmark model serves as an invaluable tool for advancing and validating algorithms for thermal runaway process monitoring, significantly enhancing the safety of the polymerization process. The effectiveness of the model and dataset is demonstrated by testing multivariate statistical process monitoring algorithms and deep learning algorithms.

Keywords: batch polymerization, bench mark modelling, thermal runaway, process monitoring

1. Introduction

Thermal runaway is a critical issue in polymerization production that demands close attention. It can lead to over-pressurization and potentially catastrophic thermal explosions. Although hazardous, the current industry-standard monitoring methods—such as temperature, pressure and inhibitor concentration monitoring(Allen, 2020)—have limitations. These methods only detect changes in individual variables and are inadequate for promptly identifying thermal runaway. Early fault detection is essential to implement effective control measures(Joy et al., 2019; Finkler et al., 2014; Gao et al., 2013) and ensure uninterrupted production. Therefore, efficient process monitoring of thermal runaway faults is necessary to enhance reliability and guarantee safe operations.

Thermal runaway is a typical incipient fault with an extended induction period(Ando et al., 2021). Multivariate statistical process monitoring (MSPM) algorithms(Cai and Tian, 2014) have been extensively studied to address this issue and maintain process safety. For instance, Pilario and Cao (2018) proposed, and Xiao (2019); Pilario et al. (2019); Wu et al. (2020) developed canonical variable dissimilarity-based fault detection algorithms. These algorithms rely on the dissimilarity between past and future canonical variables to detect process incipient faults. Kano et al. (2002) introduced the dissimilarity algorithm (DISSIM) for statistical process monitoring, which was further developed by Zhao et al. (2007, 2008, 2017); Wang and Zhao (2020). DISSIM quantitatively evaluates the differences between distributions of process data. Additionally, Harmouche et al. (2014); Chen et al. (2018); Cai and Deng (2020); Dong et al. (2022) proposed incipient fault detection and diagnosis (FDD) algorithms based on Kullback–Leibler divergence (KLD). KLD measures the dissimilarity between the probability densities of the first principal components and reference distributions obtained during normal and safe operating modes. Deep learning has gained significant traction in process monitoring in recent years. Yu and Yan (2021) developed an Intensified Iterative Learning (IIL) model based on stacked autoencoders to enhance industrial fault detection by preserving feature information. Arunthavanathan et al. (2021) proposed a novel approach for early potential fault detection using Convolutional Neural Networks (CNNs) and Long Short-Term Memory (LSTM) networks. Furthermore, Wei et al. (2022) introduced the Target Transformer model, which utilizes an attention mechanism to capture long-term dependencies in chemical processes, improving the performance of fault diagnoses. The aforementioned process monitoring algorithms are claimed to be more efficient compared to industry-standard monitoring methods.

Process monitoring algorithms plays a significant role in risk and safety management systems(Zhou et al., 2023). For instance,, Amin et al. (2021) presented a risk-based FDD methodology for nonlinear and non-Gaussian process systems based

*Corresponding author.
Email addresses: siminli@zju.edu.cn (Simin Li), yangsh@zju.edu.cn (Shuang-hua Yang), caoyi2018@zju.edu.cn (Yi Cao), jiangxiaoping@nbt.edu.cn (Xiaoping Jiang), zhou-cc@zju.edu.cn (Chenchen Zhou)

on the R-vine model. This methodology generates a risk profile of the system dynamics and effectively detects faults. The monitored risk profile detects abnormal situations, and density quantiles are used to develop a fault diagnosis module. Liu et al. (2022) proposed a Strong Relevant Mechanism Bayesian Network (SRMBN) that combines mechanism correlation analysis and process state transition. This network provides reliability analysis for risk assessment and process safety. Deng et al. (2023) introduced an improved Slow Feature Analysis (SFA) algorithm, called Probability-related Randomized SFA (PRSFA), to enhance the detection of incipient faults. Han et al. (2023) developed a traceability inference method based on a Dynamic Uncertain Causality Graph (DUCG) to identify the root cause of faults in regenerative thermal oxidizers at early anomaly alarms. This method is designed to ensure the system's operational reliability and stability.

When applying these process monitoring algorithms to a specific target application, the typical first step before conducting actual experiments is the verification of the algorithms on detailed simulation models(Annaswamy et al., 2024). The current process monitoring methods are primarily verified on benchmarks such as the Tennessee Eastman process, CSTR, or wind turbines(Downs and Vogel, 1993; Pilario and Cao, 2018; Odgaard et al., 2013). The Tennessee Eastman process simulates an industrial chemical process involving two simultaneous gas-liquid exothermic reactions. The CSTR process involves an exothermic first-order reaction. The wind turbine benchmark focuses on the system-level dynamics of wind turbines. However, validation solely on these models is insufficient to confirm their effectiveness in monitoring thermal runaway in polymerization. Thermal runaway in polymerization presents a more intricate set of mechanism factors, making detection significantly more challenging. Although several researchers(Cui et al., 2019; Liu and Wilhite, 2019, 2022; Dakkoune et al., 2018) have contributed to simulating thermal runaway, as listed in Table 1, their models have limitations. The models are not specifically designed for developing and assessing process monitoring techniques, and their proprietary nature restricts accessibility. Therefore, a new benchmark study is necessary to facilitate the development and validation of algorithms for monitoring thermal runaway in polymerization.

This work aims to bridge the gap by proposing a white-box model based on an actual industrial polymerization process with modified components, kinetics and operating conditions. The model incorporates five injectable fault types: human operation fault, inherent fault, equipment fault, sensor fault and actuator fault. Any of these can result in thermal runaway without intervention. The model equations are derived from reaction kinetics, mass balance, and energy balance analysis. With comprehensive control measures, we realize the entire production process, including the preparation, production, and final stages. To support further research, we make this model publicly available and provide a pre-processed dataset. The dataset includes 20 normal datasets and 10 fault datasets for each specific fault type. This paper provides a detailed explanation of the modelling process and offers guidelines for model usage. The model and datasets are suitable for developing and validating algorithms to monitor the thermal runaway process of polymerization. Its suitability is demonstrated through two types of process monitoring algorithm examples tested on the dataset.

In addition to algorithm development, this work is also of paramount importance in practical industrial safety. For risk engineering, the model can help identify potential hazards in the polymerization process, thereby enabling the development of strategies to manage risks across all stages of an incident. In terms of process safety, algorithms validated using this model can be applied to both laboratory testbeds and real-life experiments. This is crucial for the prompt detection of faults during actual production, significantly enhancing process safety. The main contributions of this research are as follows:

1) We first develop a novel white box model based on a simplified industrial polymerization process, which is publicly available.
2) We intentionally simulate five typical faults, which can induce thermal runaway during the production stage, to generate comprehensive fault datasets.
3) The proposed model and datasets not only facilitate the development and validation of process monitoring algorithms but also contribute to the design of control strategies and risk analysis, ultimately enhancing process safety.

In this paper, the sections are arranged as follows: Section 2 provides a detailed description of the emulsion polymerization process considered for modelling. Section 3 delves into the mathematical model and elucidates the thermal runaway fault setting. Section 4 offers insightful guidelines on how to harness this model effectively to develop robust thermal runaway process monitoring algorithms. Section 5 showcases the versatility of the proposed model in thermal runaway process monitoring by presenting a performance comparison between two distinct types of process monitoring algorithms. Lastly, Section 6 explores the potential applications and provides concluding remarks, summarizing the key findings.

2. Process description

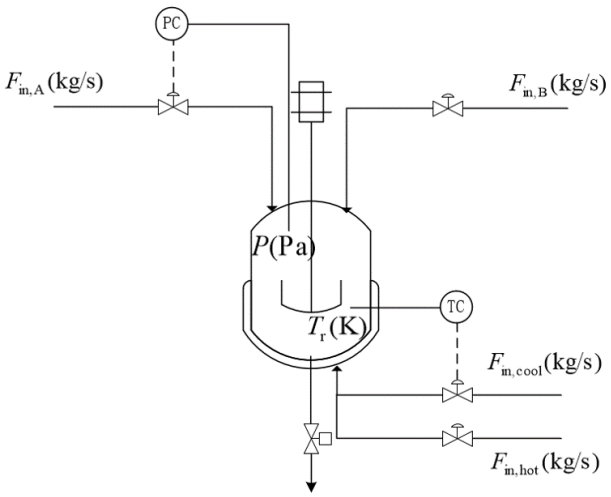

Fig. 1. Graphical description of the Semi-batch emulsion polymerization process.

Table 1: Comparison of existing thermal runaway model

Author	Modeling method	Modeling object	Application	Is model public?
Cui et al.	CFD simulation	PS	The influence of runaway conditions	No
Liu et al.	CFD simulation	PMMA	Interactions of poor mixing and exothermic chemistry	No
Liu et al.	MOM	PMMA	Design for inhibition	No
Jiang et al.	CFD simulation	PMMA	Safer operating conditions and effective inhibition	No
Dakkoune et al.	Kinetic model	Perhydrolysis of formic acid	Fault detection and isolation	No

The process under consideration involves emulsion polymerization of monomer A with initiator B, acid regulator C, and chain transfer agent E in a semi-batch industrial reactor (as illustrated in Fig. 1).

In the preparation stage, monomer A, initiator B, acid regulator C, and chain transfer agent E are simultaneously introduced to the reactor along with the entire water volume. Subsequently, the reactor is sealed, and the gas phase is evacuated to create a controlled environment.

In the production stage, heating is initiated by circulating hot water through the jacket to maintain the reactor temperature. Once a specific temperature threshold is reached, the hot water flow is stopped, and cooling water is introduced to regulate the temperature. Concurrently, the remaining monomer A and initiator B are continuously fed into the reactor to ensure a stable polymerization reaction.

In the final stage, the feeding of monomer A and initiator B is ceased after the desired cumulative amount has been delivered. Simultaneously, as the reaction progresses, the gas pressure within the batch decreases, indicating the completion of the reaction when it reaches a predetermined value.

In industrial operations, three primary control loops are employed: close-loop PID temperature control, close-loop PID pressure control, and open-loop manual reaction rate control. Pressure control is maintained by adjusting the monomer feed flow to keep a constant reactor gas pressure. Temperature control is achieved by regulating the jacket cooling water inlet flow to maintain a constant reactor temperature. Reaction rate control stabilizes the reaction rate by adjusting the initiator feed flow. The overarching objective of this intricate process is to ensure the polymerization reaction proceeds at an optimal rate while sustaining stable temperature and pressure conditions.

3. Polymerization process modelling

The primary objective of this study is to develop a comprehensive mathematical model that accurately describes the thermal runaway phenomenon in industrial polymerization production. The model description is delineated into five distinct parts: (I) Reaction model, (II) Temperature model, (III) Pressure model, (IV) Variable and parameter setting, and (V)Thermal runaway fault setting.

3.1. Reaction model

Emulsion polymerization is conceptualized as a two-phase system, consisting of a gas phase and a liquid phase. Initiator B, acid regulator C, and chain transfer agent E are predominantly present in the liquid phase, while monomer A primarily resides in the gas phase. The polymerization reaction occurs as monomer A diffuses into the liquid phase.

The polymerization process encompasses four fundamental steps: chain initiation, chain growth, chain transfer and chain termination(Farina, 1987). These sequential steps govern the formation of polymer chains during the emulsion polymerization process.

In the chain initiation stage, initiator B undergoes decomposition, resulting in the formation of active free radicals R^*. Subsequently, monomer A reacts with these active free radicals, leading to the formation of active polymer P_1. The chemical reaction equations for the chain initiation stage are as follows:

$$B \rightarrow R^*, \tag{1}$$

$$A + R^* \rightarrow P_1. \tag{2}$$

The chain growth stage involves the combination of an active polymer P_n (consisting of n chain segments) with monomer A, resulting in the formation of the active polymer P_{n+1} (now comprising $n + 1$ chain segments):

$$P_n + A \rightarrow P_{n+1}. \tag{3}$$

In the chain transfer stage, the active polymer P_n with n chain segments can undergo transfer reactions with monomer A, acid regulator C, and chain transfer agent E, resulting in the formation of the dead polymer D_n with n chain segments and corresponding active free radicals:

$$P_n + A \rightarrow D_n + P_1, \tag{4}$$

$$P_n + C \rightarrow D_n + R^*, \tag{5}$$

$$P_n + E \rightarrow D_n + R^*. \tag{6}$$

In the chain termination stage, the active polymer P_n with n chain segments and active polymer P_m with m chain segments are coupled and terminated to form a dead polymer D_{n+m} with $n + m$ chain segments:

$$P_n + P_m \rightarrow D_{n+m}. \tag{7}$$

The polymerization of A follows a free-radical mechanism. To facilitate calculations, we have simplified the reaction process. Initially, we assume equal activity among the primary free

radicals generated during each elementary reaction. Additionally, the kinetic parameters governing chain growth, chain termination, and chain transfer are assumed to be independent of chain length. Furthermore, within the considered temperature range, we exclusively account for the coupling termination reaction. Consequently, the reaction rates for each step are given by the equations below:

$$R_1 = k_{10} * e^{-\frac{E_1}{RT_r}} * [\mathrm{B}] = k_1 * [\mathrm{B}], \tag{8}$$

$$R_2 = k_{20} * e^{-\frac{E_2}{RT_r}} * [\mathrm{A}] * [\mathrm{R}^*] = k_2 * [\mathrm{A}] * [\mathrm{R}^*], \tag{9}$$

$$R_3 = k_{30} * e^{-\frac{E_3}{RT_r}} * [\mathrm{A}] * [\mathrm{P}_n] = k_3 * [\mathrm{A}] * [\mathrm{P}_n], \tag{10}$$

$$R_4 = k_{40} * e^{-\frac{E_4}{RT_r}} * [\mathrm{P}_n] * [\mathrm{A}] = k_4 * [\mathrm{P}_n] * [\mathrm{A}], \tag{11}$$

$$R_5 = k_{50} * e^{-\frac{E_5}{RT_r}} * [\mathrm{P}_n] * [\mathrm{C}] = k_5 * [\mathrm{P}_n] * [\mathrm{C}], \tag{12}$$

$$R_6 = k_{60} * e^{-\frac{E_6}{RT_r}} * [\mathrm{P}_n] * [\mathrm{E}] = k_6 * [\mathrm{P}_n] * [\mathrm{E}], \tag{13}$$

$$R_7 = k_{70} * e^{-\frac{E_7}{RT_r}} * [\mathrm{P}_n] * [\mathrm{P}_m] = k_7 * [\mathrm{P}_n] * [\mathrm{P}_m]. \tag{14}$$

Based on relevant literature and research(Sun et al., 2014), we fine-tuned the activation energies and pre-exponential factors and obtained the kinetic parameter settings shown in Table 2. It is important to emphasize that these reaction rate equations exhibit a high degree of universality when applied to other types of emulsion polymerization. However, adjustments to the relative kinetic parameters are necessary to tailor them to the specific process under investigation.

Table 2: Settings for pre-exponential factors(1/s) and activation energies(J/kmol)

Reaction label	Reaction	Pre-exponential factor	Activation energy
1	$\mathrm{B} \rightarrow \mathrm{R}^*$	$1.13 * 10^{18}$	$1.37 * 10^8$
2	$\mathrm{A} + \mathrm{R}^* \rightarrow \mathrm{P}_1$	$3.62 * 10^{13}$	$1.20 * 10^8$
3	$\mathrm{P}_n + \mathrm{A} \rightarrow \mathrm{P}_{n+1}$	$1.25 * 10^7$	$1.74 * 10^7$
4	$\mathrm{P}_n + \mathrm{A} \rightarrow \mathrm{D}_n + \mathrm{P}_1$	$3.32 * 10^6$	$5.30 * 10^7$
5	$\mathrm{P}_n + \mathrm{C} \rightarrow \mathrm{D}_n + \mathrm{R}^*$	1051	$2.00 * 10^7$
6	$\mathrm{P}_n + \mathrm{E} \rightarrow \mathrm{D}_n + \mathrm{R}^*$	1051	$2.00 * 10^7$
7	$\mathrm{P}_n + \mathrm{P}_m \rightarrow \mathrm{D}_{n+m}$	$1.38 * 10^8$	$1.36 * 10^7$

According to the principle of conservation of materials(Jokilehto, 2010), we can derive the differential equation for the change in the amount of substance for each component.

For the active free radical R^*:

$$\frac{\mathrm{d}N_{\mathrm{R}^*}}{\mathrm{d}t} = \frac{\mathrm{d}([\mathrm{R}^*]V_1)}{\mathrm{d}t} = (k_1[\mathrm{B}] - k_2[\mathrm{A}][\mathrm{R}^*] + \sum_{y=2}^{\infty}(k_5 + k_6)[\mathrm{P}_y][\mathrm{C}])V_1. \tag{15}$$

Based on relevant research, the liquid volume of the reactor is approximately linearly related to the amount of monomer in the liquid phase. Therefore, we denote $V_1 = V_{1,0} + aM_{\mathrm{A},1}$.

For monomer A:

$$\frac{\mathrm{d}N_{\mathrm{A}}}{\mathrm{d}t} = \frac{\mathrm{d}([\mathrm{A}]V_1)}{\mathrm{d}t} = (\frac{1000F_{\mathrm{gl}}}{M_{\mathrm{A}}V_1} - k_2[\mathrm{A}][\mathrm{R}^*] - \sum_{y=2}^{\infty}(k_3 + k_4)[\mathrm{A}][\mathrm{P}_y])V_1. \tag{16}$$

For initiator B:

$$\frac{\mathrm{d}N_{\mathrm{B}}}{\mathrm{d}t} = \frac{\mathrm{d}([\mathrm{B}]V_1)}{\mathrm{d}t} = (\frac{1000F_{\mathrm{in,B}}}{M_{\mathrm{B}}V_1} - k_1[\mathrm{B}])V_1. \tag{17}$$

For acid regulator C:

$$\frac{\mathrm{d}N_{\mathrm{C}}}{\mathrm{d}t} = \frac{\mathrm{d}([\mathrm{C}]V_1)}{\mathrm{d}t} = (-\sum_{y=2}^{\infty}k_5[\mathrm{C}][\mathrm{P}_y])V_1. \tag{18}$$

For chain transfer agent E:

$$\frac{\mathrm{d}N_{\mathrm{E}}}{\mathrm{d}t} = \frac{\mathrm{d}([\mathrm{E}]V_1)}{\mathrm{d}t} = (-\sum_{y=2}^{\infty}k_6[\mathrm{E}][\mathrm{P}_y])V_1. \tag{19}$$

For active polymer with a chain length of $n = 1$:

$$\frac{\mathrm{d}N_{\mathrm{P}_1}}{\mathrm{d}t} = \frac{\mathrm{d}([\mathrm{P}_1]V_1)}{\mathrm{d}t} = (k_2[\mathrm{A}][\mathrm{R}^*] - k_3[\mathrm{A}][\mathrm{P}_1] + \sum_{y=2}^{\infty}k_4[\mathrm{A}][\mathrm{P}_y])V_1. \tag{20}$$

For active polymer with a chain length of $n \geq 2$:

$$\begin{aligned}\frac{\mathrm{d}N_{\mathrm{P}_n}}{\mathrm{d}t} = \frac{\mathrm{d}([\mathrm{P}_n]V_1)}{\mathrm{d}t} =& (k_3[\mathrm{A}]([\mathrm{P}_{n-1}] - [\mathrm{P}_n]) - k_4[\mathrm{A}][\mathrm{P}_n] - k_5[\mathrm{P}_n][\mathrm{C}] \\ &- k_6[\mathrm{P}_n][\mathrm{E}] - \sum_{y=2}^{\infty}k_7[\mathrm{P}_y][\mathrm{P}_n])V_1.\end{aligned} \tag{21}$$

For dead polymer with a chain length of $n \geq 2$:

$$\begin{aligned}\frac{\mathrm{d}N_{\mathrm{D}_n}}{\mathrm{d}t} = \frac{\mathrm{d}([\mathrm{D}_n]V_1)}{\mathrm{d}t} =& (k_4[\mathrm{A}][\mathrm{P}_n] + k_5[\mathrm{P}_n][\mathrm{C}] + k_6[\mathrm{P}_n][\mathrm{E}] \\ &+ \sum_{y=2}^{\frac{n}{2}}k_7[\mathrm{P}_j][\mathrm{P}_{n-y}])V_1.\end{aligned} \tag{22}$$

Since the chain length n can be very large, the number of differential equations for the concentration variation of active polymers is infinite. To facilitate the calculation, the method of moments is introduced, which converts infinite differential equations to finite ones. We denote

$$\lambda_m = \sum_{n=1}^{\infty}n^m[\mathrm{P}_n], \tag{23}$$

$$\mu_m = \sum_{n=2}^{\infty}n^m[\mathrm{D}_n]. \tag{24}$$

Therefore, the moment equations can be listed as

$$\frac{\mathrm{d}(\lambda_0 V_1)}{\mathrm{d}t} = (k_2[\mathrm{A}][\mathrm{R}^*] - (k_5[\mathrm{C}] + k_6[\mathrm{E}])\lambda_0 - k_7\lambda_0^2)V_1, \tag{25}$$

$$\begin{aligned}\frac{\mathrm{d}(\lambda_1 V_1)}{\mathrm{d}t} =& (k_2[\mathrm{A}][\mathrm{R}^*] + (k_3 + k_4)[\mathrm{A}]\lambda_0 - (k_4[\mathrm{A}] + k_5[\mathrm{P}_j][\mathrm{C}] \\ &+ k_6[\mathrm{E}])\lambda_1 - k_7\lambda_0\lambda_1)V_1,\end{aligned} \tag{26}$$

$$\begin{aligned}\frac{\mathrm{d}(\lambda_2 V_1)}{\mathrm{d}t} =& (k_2[\mathrm{A}][\mathrm{R}^*] + (k_3 + k_4)[\mathrm{A}]\lambda_0 + 2k_3[\mathrm{A}]\lambda_1 \\ &- (k_4[\mathrm{A}] + k_5[\mathrm{P}_j][\mathrm{C}] + k_6[\mathrm{E}])\lambda_2 - k_7\lambda_0\lambda_2)V_1,\end{aligned} \tag{27}$$

$$\frac{\mathrm{d}(\mu_0 V_1)}{\mathrm{d}t} = ((k_4C_{\mathrm{A}} + k_5C_{\mathrm{C}} + k_6C_{\mathrm{E}})\lambda_0 + \frac{1}{2}k_7\lambda_0^2)V_1, \tag{28}$$

$$\frac{\mathrm{d}(\mu_1 V_1)}{\mathrm{d}t} = ((k_4C_{\mathrm{A}} + k_5C_{\mathrm{C}} + k_6C_{\mathrm{E}})\lambda_1 + k_7\lambda_0\lambda_1)V_1, \tag{29}$$

$$\frac{\mathrm{d}(\mu_2 V_1)}{\mathrm{d}t} = ((k_4C_{\mathrm{A}} + k_5C_{\mathrm{C}} + k_6C_{\mathrm{E}})\lambda_2 + k_7(\lambda_0\lambda_2 + \lambda_1^2))V_1. \tag{30}$$

The differential equation for the amount-of-substance change of each component can be expressed by moments.

For active free radicals R^*:

$$\frac{dN_{R^*}}{dt} = \frac{d([R^*]V_l)}{dt} = (k_1[B] - k_2[A][R^*] + k_5[C]\lambda_0 + k_6[E]\lambda_0)V_l. \tag{31}$$

For monomer A:

$$\frac{dN_A}{dt} = \frac{d([A]V_l)}{dt} = (\frac{1000F_{gl}}{M_A V_l} - k_2[A][R^*] - (k_3 + k_4)[A]\lambda_0)V_l. \tag{32}$$

For acid regulator C:

$$\frac{dN_C}{dt} = \frac{d([C]V_l)}{dt} = (-k_5[C]\lambda_0)V_l. \tag{33}$$

For chain transfer agent E:

$$\frac{dN_E}{dt} = \frac{d([E]V_l)}{dt} = (-k_6[E]\lambda_0)V_l. \tag{34}$$

The reaction rate R_A is defined as the A monomer consumption rate in the reactor, which can be calculated as

$$R_A = (k_2[A][R^*] + (k_3 + k_4)[A]\lambda_0)V_l. \tag{35}$$

The number average molecular weight $\overline{M}_n$ and the weight average molecular weight $\overline{M}_w$ can be calculated by the following equations:

$$\overline{M}_n = M_A\frac{\mu_1 + \lambda_1}{\mu_0 + \lambda_0}, \tag{36}$$

$$\overline{M}_w = M_A\frac{\mu_2 + \lambda_2}{\mu_1 + \lambda_1}. \tag{37}$$

3.2. Temperature model

The heat transfer process in polymerization can be divided into two parts: jacket and reactor transfer. Based on the assumption that the reactor and the jacket are well-mixed, the dynamic heat balance of the stirred tank reactor and external jacket is written as

$$(M_s C_{p,s} + M_A C_{p,A})\frac{dT_r}{dt} = Q_{feed} + Q_w + Q_r + Q_{stir} - Q_{loss}, \tag{38}$$

$$M_j C_{p,j}\frac{dT_j}{dt} = Q_{in,j} - Q_{out,j} - Q_w. \tag{39}$$

In Equation (38), the left side is the term describing the heat accumulation in the reactor. The heat change of initiators and other additives is assumed to be negligible. On the right side of the equation, Q_{feed} is the heat input due to the feeds, Q_w is the heat flow through the reactor wall, Q_r is the reaction heat, Q_{stir} is the energy input due to the stirrer, Q_{loss} is the heat loss to the surroundings, and M is the mass of the reactor contents.

The presence of Q_{feed} is due to the temperature difference between the monomer feed and the reactor. It can be calculated as

$$Q_{feed} = F_{in,A}C_{p,A}(T_A - T_r). \tag{40}$$

Under steady-state conditions, the heat flow through the reactor wall is given by

$$Q_w = US(T_j - T_r). \tag{41}$$

Chain growth plays a dominant role in the polymerization process. Assuming that the heat of reaction is equal to the heat released by chain growth, the heat of reaction is

$$Q_r = \Delta H k_3[A]\lambda_0 V_l. \tag{42}$$

As Q_{loss} is a result of evaporation and condensation processes, it is influenced by the geometry of the reactor and the temperature difference between the reaction mixture and its surroundings. n empirical formula is used, considering the ambient temperature and the reaction temperature:

$$Q_{loss} = b_1(T_r - T_{amb})^{b_2}. \tag{43}$$

The energy input by stirring is computed by:

$$Q_{stir} = K\rho N^3 d^5. \tag{44}$$

Stirrer heat is estimated at 0.5 W, which is negligible and therefore excluded from further calculations.

Therefore, the temperature change of the reactor can be calculated as follows:

$$\begin{aligned}\frac{dT_r}{dt} =&(F_{in,A}C_{p,A}(T_A - T_r) + US(T_j - T_r) + \Delta H * k_3[A]\lambda_0 V_l \\ &- b_1(T_r - T_{amb})^{b_2} + Q_{stir})/(M_s C_{p,s} + M_A C_{p,A}).\end{aligned} \tag{45}$$

In Equation (39), the left side of the equation describes how much heat accumulates in the jacket media mass. On the right side, $Q_{in,j}$ represents the heat input due to the jacket feeds, $Q_{out,j}$ is the heat output and Q_w is the heat flow through the reactor wall.

$Q_{in,j}$ and $Q_{out,j}$ are included in the equation because jacket heat exchange is a continuous process. These values are defined as

$$Q_{in,j} = F_j C_{p,j} T_{in,j}, \tag{46}$$

$$Q_{out,j} = F_j C_{p,j} T_j. \tag{47}$$

Thus, the temperature change of the jacket can be calculated as

$$\frac{dT_j}{dt} =(F_j C_{p,j}(T_{in,j} - T_j) - US(T_j - T_r))/M_j C_{p,j}. \tag{48}$$

3.3. Pressure model

According to the ideal gas lawLearning (2021) $PV = nRT$, the change of reactor gas pressure can be expressed as

$$\frac{d(PV_g)}{dt} = R(T_r\frac{dN_{g,A}}{dt} + N_{g,A}\frac{dT_r}{dt}). \tag{49}$$

Since $\frac{dT_r}{dt}$ has already been calculated in previous section, we now need to determine $\frac{dN_{g,A}}{dt}$. The change in $N_{g,A}$ is the

difference between the A monomer feed rate $F_{\text{in,A}}$ and the A dissolution rate in the liquid phase F_{gl}:

$$\frac{\mathrm{d}N_{\text{g,A}}}{\mathrm{d}t} = \frac{1000}{M_{\text{A}}}(F_{\text{in,A}} - F_{\text{gl}}). \tag{50}$$

According to the solute penetration model(Abraham et al., 1995), F_{gl} can be calculate using the following equation:

$$F_{\text{gl}} = k([\text{A}]_0 - [\text{A}]) = k(\frac{P}{H} - [\text{A}]) \tag{51}$$

where Henry's law(Sander, 2015) states that $[\text{A}]_0 = \frac{P}{H}$. In this paper we assume k to be constant as the temperature variation is minimal.

By combining Equation (50) and (51), we obtain

$$\frac{\mathrm{d}N_{\text{g,A}}}{\mathrm{d}t} = \frac{1000}{M_{\text{A}}}(F_{\text{in,A}} - k(\frac{P}{H} - [\text{A}])). \tag{52}$$

Therefore, the pressure change of the reactor can be calculated as follows:

$$\frac{\mathrm{d}(PV_{\text{g}})}{\mathrm{d}t} = \text{R}(N_{\text{g,A}}\frac{\mathrm{d}T_{\text{r}}}{\mathrm{d}t} + \frac{1000T_{\text{r}}}{M_{\text{A}}}(F_{\text{in,A}} - k(\frac{P}{H} - [\text{A}]))). \tag{53}$$

3.4. Variable and parameter setting

The process has four manipulated variables and seven measured variables as listed in Table 3-4. Disturbances are introduced to each manipulated variable, and noises are added to each measured variable. All disturbances and noises follow a normal distribution, and relative variances can be found in Table 3-4. Relative parameter values are given in Table 5.

Table 3: Disturbances in the manipulated variables

Variable	Description	Variance	Units
$F_{\text{in,A}}$	Monomer A feed rate	10^{-4}	kg/s
$F_{\text{in,B}}$	Initiator B feed rate	10^{-16}	kg/s
$T_{\text{j,in}}$	Jacket water inlet temperature	1	K
F_{j}	Jacket water inlet flow	0.01	kg/s

Table 4: Noises in the measured variables

Variable	Description	Variance	Units
[A]	A concentration	10^{-4}	mol/L
[B]	B concentration	10^{-14}	mol/L
[C]	C concentration	10^{-15}	mol/L
[E]	E concentration	10^{-15}	mol/L
T_{r}	reactor temperature	10^{-3}	K
P	reactor pressure	10^{7}	Pa
R_{A}	reaction rate	100	kg/h

3.5. Thermal runaway fault setting

In this benchmark model, several faults are considered, covering different kinds of possible faults in the polymerization process. Table 6 summarizes the five introduced typical fault scenarios. Fault 1 corresponds to a sudden change in initiator feed, while the remaining faults exhibit gradual drifts. Although these faults vary in severity, they may all lead to thermal runaway. Different fault simulations can be achieved using specific switches.

Fault 1: Change in initiator feed. In this polymerization process, the addition of initiator is controlled based on artificial experience. To ensure reaction rate stability, we adopted a two-stage initiator feeding strategy: faster during the ramp-up phase and slower to maintain a steady rate. However, due to operator inexperience, a delayed switching could result in an excessive initiator addition, leading to increased reaction rate and potential thermal runaway.

Normally, the initiator feed is changed at 5300s. But in the fault scenario, this change is delayed by 1140 seconds. A human operation fault resulting in a step change in the initiator feed rate can deviate the initiator concentration, [B], from the desired level in the reactor. An excessive initiator can increase the chain initiation rates, R_1 and R_2, subsequently enhancing the chain growth rate, R_3. This acceleration of the initiation and growth rates ultimately elevates the reaction rate, R_{A}. The increased reaction rate generates excess heat, Q_{r}, causing a rise in the reactor temperature, T_{r}.

Fault 2: Gel effect. During the polymerization process, as the reaction proceeds, monomers gradually transform into polymers, leading to an increase in the viscosity of the reaction system. When the viscosity of the reaction system reaches a critical point, the system transitions from a flowing liquid to a viscous syrup. Consequently, chain segments encounter significant resistance during rearrangement. Active free radicals at the chain ends experience challenges in reacting with other chain-end radicals for termination, resulting in a significant reduction in the termination rate constant. However, the active free radicals at the chain ends persist, and the system's viscosity does not impede monomer diffusion sufficiently to halt the polymerization reaction.

Marten and Hamielec (1982) propose a modelling of the gel effect, denoting as $I = \overline{M}_w^{c_1} e^{\frac{G}{V_{\text{f}}}}$ and I_3 is the critical judgment value of Gel effect. In this model, when the reaction starts, $I<I_3$ and $k_{7,\text{real}} = k_7$. As the reaction progresses, the I value

Table 5: Constant values in the mathematical model

Parameter	Description	Value	Units
$C_{\text{p,A}}$	Monomer heat capacity	804	J/(kg ∗ K)
US	Heat transfer coefficient	16870	W/K
ΔH	Standard reaction heat	172700	J/mol
$V_{\text{l,0}}$	Liquid volume	2	m^3
V	Reactor volume	6	m^3
T_{amb}	Environment temperature	293	K
T_{A}	Inlet monomer temperature	333	K
Q_{stir}	Stirring heat	0.5	W
M_{s}	Mass of reactor liquid phase	2000	kg
M_{j}	Mass of jacket water	2000	kg
$C_{\text{p,s}}, C_{\text{p,j}}$	Heat capacity	4200	J/(kg ∗ K)
R	Ideal gas constant	8.314	J/(mol ∗ K)
a	Coefficient	0.667	/
b_1	Coefficient	1	/
b_2	Coefficient	2	/
k	Coefficient	0.0562	/
H	Coefficient	700	/

Table 6: Fault scenarios in the mathematical model

Fault	Description	Type	Classification
1	Change in initiator feed	step	Human operation fault
2	Gel effect	slow drift	Inherent fault
3	Heat transfer fouling	slow drift	Equipment fault
4	Inaccurate thermometer	slow drift	Sensor fault
5	Jacket cooling water valve sticky	slow drift	Actuator fault

gradually increases. When I exceeds I_3, the Gel effect occurs, and $k_{7,\text{real}}$ can be calculated as

$$\frac{k_{7,\text{real}}}{k_7} = \left(\frac{\overline{M}_{\text{wcr}}}{\overline{M}_{\text{w}}}\right)^{c_2} e^{-G\left(\frac{1}{V_{\text{f}}} - \frac{1}{V_{\text{fcr}}}\right)}. \tag{54}$$

The free volume fraction, V_{f}, is calculated as

$$V_{\text{f}} = 0.025 + \Delta\alpha_{\text{p}}(T_{\text{r}} - T_{\text{gp}})\phi_{\text{p}} + \Delta\alpha_{\text{M}}(T_{\text{r}} - T_{\text{gM}})\phi_{\text{M}} \tag{55}$$

where $\phi_{\text{p}} = \frac{(1+\epsilon)X}{1+\epsilon X}$ and $\phi_{\text{M}} = 1 - \phi_{\text{p}}$.

This is an inherent fault characterized by a slow drift change in the chain termination rate constant, k_7. According to the polymerization rate equation, the termination rate constant, k_7, undergoes a gradual decrease, while the chain growth rate constant, k_3, remains nearly constant. Consequently, the ratio of k_3 to k_7 increases substantially. Given the positive correlation between the polymerization reaction rate, R_{A}, and this ratio, there is a significant elevation in the reaction rate. The increased reaction rate generates excess heat, Q_{r}, resulting in a rise in the reactor temperature, T_{r}.

Fault 3: Heat transfer fouling. In the reaction stage, a viscous product is produced. Heat transfer coefficients are reduced if products adhere to reactor walls, which leads to reduced heat transfer capacity of the jacket. If the rate of heat generation from the reaction exceeds the jacket's maximum heat transfer capacity, thermal runaway will occur.

Here, we denote $US_{\text{real}} = US - c_3 t$ representing an equipment fault that leads to a gradual reduction in the heat transfer coefficient. As US_{real} decreases, the heat flow through the reactor wall, Q_{w}, decreases, resulting in an increase in reactor temperature, T_{r}.

Fault 4: Inaccurate thermometer. There are several reasons for inaccurate thermometer readings. The first is electrical or mechanical faults in the temperature sensor. Additionally, any products attached to the temperature sensor can impact temperature measurements. These faults can introduce a fixed offset or a gain factor in measurements. An inaccurate thermometer can disrupt temperature control and potentially lead to thermal runaway.

Here, we denote $T_{\text{r,real}} = T_{\text{r}} - c_{4,1}t - c_{4,2}$. If $c_{4,1} \neq 0$ and $c_{4,2} = 0$, it can perform a gain factor in measurement. If $c_{4,1} = 0$ and $c_{4,2} \neq 0$, it can perform a fixed offset in measurement. In this model, we set $c_{4,2} = 0$ to monitor a sensor fault characterized by a slow drift change. This fault causes the measured reactor temperature, T_{r}, to be lower than and deviate gradually from the actual reactor temperature, $T_{\text{r,real}}$. The incorrect temperature measurement leads to untimely feedback and adjustment of the jacket cooling water flow, F_{j}, by the temperature controller, reducing the efficiency of the jacket heat exchange, Q_{w}. Consequently, despite insignificant changes in the measured temperature, the real reactor temperature, $T_{\text{r,real}}$, has already exceeded the control range.

Fault 5: Jacket cooling water valve sticky. The phenomenon of hydraulic valve body sticking typically occurs due to increased friction as the valve core moves. This is known as

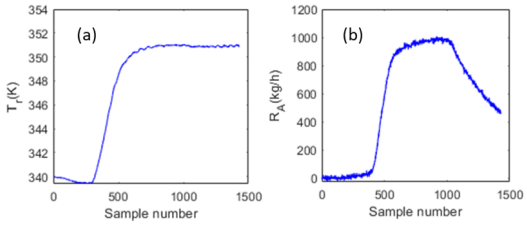

Fig. 2. Trends of sample at normal condition: (a)T_{r} at normal condition, (b)R_{A} at normal condition.

"damped sticking", where small particles accumulate between the hydraulic valve core and the valve body, resulting in increased friction of the valve core. Damped sticking leads to a decreased response speed of the valve. If the jacket cooling water valve becomes sticky, adjustments in cooling water flow may be delayed, affecting heat exchange and potentially causing thermal runaway.

Here, we denote $F_{\text{j,real}} = F_{\text{j}} - c_5 t$, representing an actuator fault with a slow drift change. This fault causes the actual jacket cooling water flow, $F_{\text{j,real}}$, to be lower than and gradually deviate from the intended control output, F_{j}. Consequently, the efficiency of the jacket heat exchange, Q_{w}, decreases, leading to an increase in the reactor temperature, T_{r}, as described by Equation (38). Relative parameter values can be found in Table 7.

Table 7: Model parameters in fault setting

Parameter	Value	Units
T_{gM}	167	K
T_{gp}	383	K
$\Delta\alpha_{\text{M}}$	10^{-3}	K^{-1}
$\Delta\alpha_{\text{p}}$	$4.8 * 10^{-4}$	K^{-1}
I_3	$e^{-0.4+\frac{4460}{T_{\text{r}}}}$	/
ϵ	$\frac{0.966471-1.164*10^{-3}T_{\text{r}}}{1.19504-3.3*10^{-4}T_{\text{r}}} - 1$	/
G	1.11	/
c_1	0.5	/
c_2	1.75	/
c_3	30	$\text{W}/(\text{K} * \text{s})$
$c_{4,1}$	0.0001	K/s
$c_{4,2}$	0	K
c_5	0.013	kg/s^2

The polymerization process and thermal runaway faults simulation model is available online(Li, 2024). Fig. 2 illustrates the simulation results under normal operating conditions. As shown, the reaction temperature steadily increases to a peak of 351 K and is then maintained at this level by the reaction temperature controller. Simultaneously, the reaction rate is held steady within a range of 900–1000 kg/h. Relative thermal runaway simulation results are shown in Fig. 3. It can be observed that when a fault occurs, the reaction rate and reactor temperature initially remain stable at the beginning. However, as the fault progresses significantly, the reaction rate and reactor temperature increase rapidly, leading to thermal runaway.

The exothermic nature of the polymerization reaction plays a critical role in understanding these faults. Faults 1 and 2 contribute to an increase in heat release, whereas faults 3, 4, and 5 reduce the heat transfer capacity of the jacket. Initially, when a fault occurs, the heat release rate is within the jacket's heat transfer capacity, resulting in a relatively stable reactor temper-

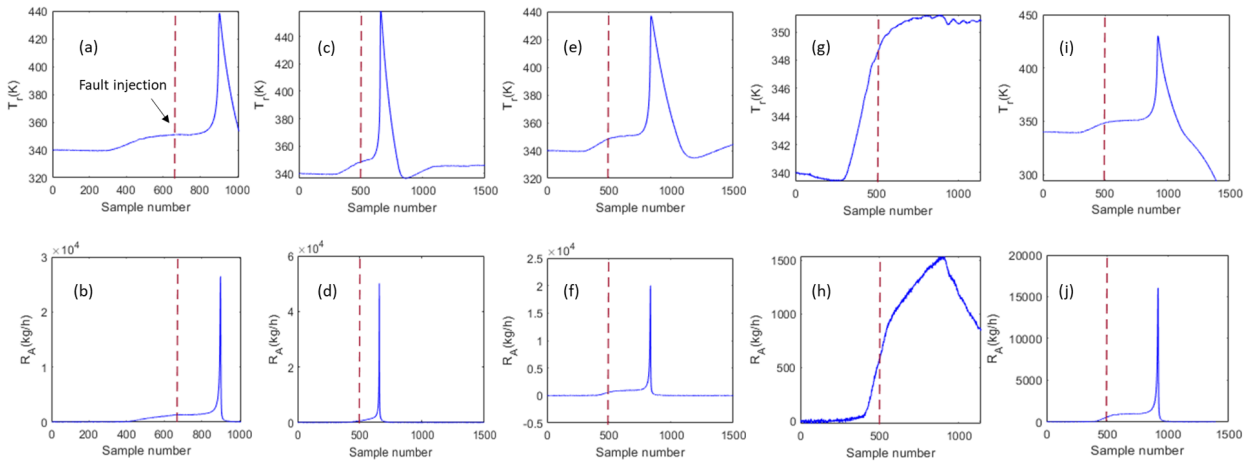

Fig. 3. Trends of sample at different fault condition: (a)T_r of Fault 1, (b)R_A of Fault 1, (c)T_r of Fault 2, (d)R_A of Fault 2, (e)T_r of Fault 3, (f)R_A of Fault 3, (g)T_r of Fault 4, (h)R_A of Fault 4, (i)T_r of Fault 5, (j)R_A of Fault 5. Legend: Red Dash dot-start of fault.

ature. However, as the fault intensifies, the exothermic reaction rate surpasses the jacket's cooling capacity, causing a rise in the reaction temperature. This temperature increase, coupled with the positive feedback loop between reaction temperature and rate, can ultimately lead to thermal runaway. If thermal runaway is not handled properly, it may cause product loss at the very least, or even exposition, personal injury or death. Therefore, employing process monitoring algorithms to promptly detect faults and prevent the escalation of positive feedback and thermal runaway is crucial. The simulation results are confirmed to be similar to the actual production process. However, due to confidentiality principles, we are unable to provide specific data on the actual process.

4. Use of the model for algorithm development

4.1. Data generation and preprocessing

The model file(Li, 2024) includes partially preprocessed normal and faulty datasets, without data normalization. Normal condition has 20 datasets while each fault has 10 faulty datasets. Each dataset represents a complete batch process, organized as an 11-column matrix. The manipulated variables, variables, $\boldsymbol{u} = [F_\mathrm{A}\ F_\mathrm{B}\ F_\mathrm{j}\ T_\mathrm{in,j}]$, are represented by the first four columns, while the last seven columns represent the measured variables, $\boldsymbol{y} = [[\mathrm{A}]\ [\mathrm{B}]\ [\mathrm{C}]\ [\mathrm{E}]\ T_\mathrm{r}\ P\ R_\mathrm{A}]$. Each row is a sample taken at 10-second intervals. We encourage readers to run the model themselves and collect data using the operation manual provided in the open access link, which contains more detailed informations about this model.

Data generation. To establish the model conditions, the solver, relative tolerance, maximum simulation time, and normal/fault conditions were specified. The model was then run multiple times, and the data was obtained in the MATLAB workspace for subsequent analysis.

Data filtering. The sampling interval was determined, and the data was filtered to acquire the normal and faulty datasets with a fixed sampling rate.

Data alignment. Various methods, including head alignment, dynamic time warping (DTW), and others, can be used to align multiple training datasets in the time direction. These methods ensure data synchronization, enabling effective training and comparison across different datasets

Data normalization. To ensure an equal contribution of each variable during dimensionality reduction, the datasets ware normalized. This was achieved by calculating the mean and variance of each variable and scaling the data so that the mean becomes zero and the variance equals one.

Normalization involves two steps. As the first step, we subtract the sample mean of each variable:

$$\boldsymbol{X}_\mathrm{mean} = \frac{1}{20}\sum_{i=1}^{20}\boldsymbol{X}_i. \tag{56}$$

Second, we scale each variable to unit variance:

$$\overline{\boldsymbol{X}}_i = (\boldsymbol{X}_i - \boldsymbol{X}_\mathrm{mean})/\boldsymbol{X}_\mathrm{st}. \tag{57}$$

Subsequently, we expand the three-dimensional normal datasets along the batch direction for ease of calculation, as shown in Fig. 3.

$$\boldsymbol{X}_\mathrm{train} = \left[\overline{\boldsymbol{X}}_1; \overline{\boldsymbol{X}}_2; \cdots; \overline{\boldsymbol{X}}_{20}\right]. \tag{58}$$

For new sample, the normalization procedure is similar:

$$\boldsymbol{x}_{\mathrm{test},k} = (\boldsymbol{x}_k - \boldsymbol{x}_\mathrm{mean})/\boldsymbol{x}_\mathrm{st}. \tag{59}$$

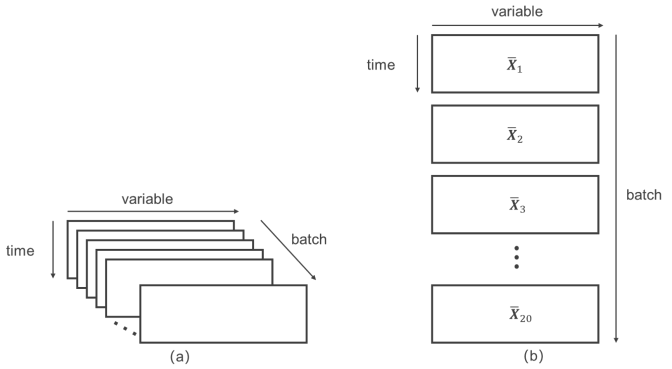

Fig. 3. Graphical description of three dimensional expansion. (a)before expansion (b)after expansion.

4.2. Process monitoring algorithm selection

In this part, we choose appropriate process monitoring algorithms to enable early fault detection, diagnosis of root causes, and severity assessment. The goal is to prevent potential failures or system shutdowns by providing timely identification and understanding of faults.

MSPM algorithms. Statistical process monitoring algorithms utilize time-series features extracted through multivariate approaches for fault detection, identification, and reconstruction. Monitoring statistics, such as Hotelling's T2 and the squared prediction error (SPE), can be calculated from these time-series features to detect faults. Associated thresholds are defined for comparison with the monitoring statistics. Upon fault detection, contribution plots help identify the process variables that significantly impact the fault occurrence.

Machine learning algorithms. Unsupervised learning algorithms, such as clustering analysis, can detect anomalies, including faulty conditions or new normal operating states. This is achieved by analysing unlabelled raw data and identifying patterns without predefined labels. In contrast, supervised classification and regression algorithms rely on labelled data and extracted features to accurately detect, diagnose, and assess the severity of faults. In the context of the benchmark dataset, labeling can be performed using a priori normal/fault information during the pre-processing stage.

4.3. Performance evaluation

We evaluate monitoring results using three performance indices: fault detection rate (FDR), fault detection time (FDT), and false alarming rate (FAR). Specifically, the FDR, as represented by Equation (60), signifies the proportion of samples that exceed the control limit relative to all actual faulty samples. On the other hand, the FDT denotes the time interval between the introduction of a fault and its initial detection. We define the FAR, as given by Equation (61), as the fraction of samples that surpass the control limit among all normal samples.

$$\text{FDR} = \frac{N_{FP}}{N_{FP} + N_{TN}} \times 100\%, \tag{60}$$

$$\text{FAR} = \frac{N_{FN}}{N_{TP} + N_{FN}} \times 100\%. \tag{61}$$

5. Demonstration of process monitoring algorithms on the model

5.1. MSPM algorithms

As polymerization is a dynamic process, it's better to choose dynamic MSPM techniques such as canonical variate analysis (CVA). Furthermore, it has been concluded that canonical variate dissimilarity analysis (CVDA) outperforms traditional CVA methods and other dissimilarity-based methods, like KLD, DISSIM, and growing curvilinear component analysis (GCCA)(Safaeipour et al., 2021). Therefore, CVDA and its relevant algorithms, mixed-kernel canonical variate dissimilarity analysis (MK-CVDA), and canonical variate dissimilarity and mixed-kernel principal component analysis (CVD-MKPCA), are employed to monitor the five thermal runaway faulty processes.

The Gaussian kernel function (Equation (62)) is utilized for kernel expansion:

$$k(\boldsymbol{x}_i, \boldsymbol{x}_j) = \exp(-\frac{||\boldsymbol{x}_i - \boldsymbol{x}_j||^2}{h}) \tag{62}$$

with an empirically determined kernel width of $h = 50m$. We find that a maximum of three lags is significant at the 5% confidence level; thus, the past and future measurements are set to 3. To ensure minimal information loss, the number of reserved canonical variables is set to capture approximately 90% of the total sum of eigenvalues or singular values. Control limits are calculated with 95% confidence using kernel density estimation. Any four consecutive samples exceeding the control limit are classified as faults.

5.2. Deep learning algorithms

With the rapid advancement of artificial intelligence, deep learning has found increasingly extensive applications in process monitoring. Among the myriad deep learning algorithms, CNNs have been prominently applied to fault diagnosis. The hallmark feature of CNNs is their weight-sharing convolutional structure, which reduces model complexity and the number of parameters, thereby effectively mitigating the issue of over-fitting. However, CNNs do not inherently capture long-term dependencies in sequential data over time. This limitation is addressed by LSTM networks, which are specifically designed to process time series data and learn long-term dependencies. Consequently, the employment of both CNN and LSTM algorithms is warranted in monitoring the five thermal runaway fault processes.

Table 8 illustrates the architectural designs of the CNN and LSTM neural networks. The CNN architecture comprises 3 convolutional layers, 3 max pooling layers, and 2 fully connected (FC) layers. Conversely, the LSTM architecture includes 1 LSTM layer and 3 FC layers. To facilitate training, the dataset was randomly partitioned into three subsets: a training set, a validation set, and a test set. Specifically, the training set encompassed 14 normal datasets and 3 datasets per fault type, while the validation set contained 6 normal datasets and 2 datasets per fault type. The test set contains 5 datasets for each fault type.

Table 8: Neural networks for fault detection of the proposed model

Neural network	Architecture
CNN	Conv(8)-Pool(2)-Conv(16)-Pool(2)-Conv(32)-Pool(2)-FC(64)–FC(6)
LSTM	Lstm(120)-FC(64)–FC(6)

5.3. Monitoring results

Table 9-11 presents the average FDRs, FDTs, and FARs across five fault scenarios, calculated over ten tests. Initially, We focus on the MSPM algorithms. From Table 11, all MSPM algorithms exhibit lower FARs. When comparing CVDA and CVA in Table 10, it is evident that CVDA detects faults earlier, suggesting that dissimilarity analysis is more sensitive to minor fault variations. Additionally, Nonlinear feature-based algorithms outperform those based on linear features. For example, MK-CVDA and CVD-MKPCA detect faults significantly earlier than CVA and CVDA. Specifically, CVD-MKPCA yields shorter FDTs for Fault 1,2,4 and 5, while MK-CVDA showing improved results for the Fault 3 scenario.In the following discussion, we focus on a comparative analysis between nonlinear feature-based methods, namely MK-CVDA and CVD-MKPCA. While MK-CVDA demonstrates superior FDRs and FDTs for Fault 3, CVD-MKPCA consistently outperforms other methods across Faults 1, 2, 4, and 5. The results in Table 9-11 reinforce the conclusion that CVD-MKPCA surpasses other methods for almost all faults. This aligns with findings from a CSTR case study in a previous article(Wu et al., 2020), further support for the effectiveness of our proposed model.

Table 9: Comparison of fault detection rates for the five faults in batch polymerization process

Algorithm	CVA	CVDA	MK-CVDA	CVD-MKPCA	CNN	LSTM
Fault 1	98.66%	99.23%	99.24%	99.55%	100%	98.64%
Fault 2	96.40%	96.80%	96.83%	96.87%	95.62%	96.93%
Fault 3	84.85%	86.57%	88.16%	86.05%	78.75%	86.05%
Fault 4	95.07%	95.76%	96.46%	96.61%	92.02%	95.60%
Fault 5	86.20%	81.09%	86.98%	89.10%	78.07%	98.15%

Table 10: Comparison of fault detection times(samples) for the five faults in batch polymerization process

Algorithm	CVA	CVDA	MK-CVDA	CVD-MKPCA	CNN	LSTM
Fault 1	8	5	5	4	1	1
Fault 2	32	30	28	25	40	28
Fault 3	36	33	30	33	186	52
Fault 4	28	22	17	22	45	25
Fault 5	38	35	35	32	160	46

We subsequently evaluated the performance of deep learning algorithms, including CNN and LSTM. During network training, the accuracy of CNN and LSTM exhibited similar values, with CNN achieving 93.09% and LSTM attaining 93.50%. However, LSTM demonstrated superior performance compared to CNN regarding FDRs and FDTs. Specifically, LSTM yielded higher FDRs and lower FDTs for Faults 2, 3, 4, and 5. The ability of both CNN and LSTM to detect Fault 1 at its first occurrence may be attributed to the subtle differences between Fault 1 and normal conditions, which may have led to inaccurate classification during training and subsequently resulted in a high FAR. Notably, all other faults maintained a low false alarm rate. In summary, LSTM outperforms CNN in monitoring thermal runaway faults in the polymerization process, emphasizing the importance of capturing long-term dependencies.

Table 11: Comparison of false alarm rates for the five faults in batch polymerization process

Algorithm	CVA	CVDA	MK-CVDA	CVD-MKPCA	CNN	LSTM
Fault 1	1.76%	1.58%	2.77%	1.71%	11.87%	15.91%
Fault 2	0.91%	1.41%	1.33%	1.62%	0	0
Fault 3	0.87%	1.41%	1.79%	1.21%	0	0.12%
Fault 4	1.79%	1.79%	2.35%	1.82%	0	0.44%
Fault 5	2.01%	1.37%	2.23%	2.42%	0	0.12%

CVD-MKPCA and LSTM exhibit comparable FDRs, but CVD-MKPCA demonstrates greater sensitivity to most faults. More advanced network structures can be designed for the LSTM algorithm to enhance its sensitivity to faults further. MSPM and deep learning algorithms have their own advantages and disadvantages. MSPM algorithms require a smaller number of normal samples for training compared to deep learning algorithms, whereas deep learning algorithms can leverage both normal and fault samples to train more accurate models. The choice of a specific algorithm depends on the particular requirements and constraints of the problem at hand.

6. Discussions and conclusions

6.1. Discussions

The proposed benchmark model can be used for studying several problems:

6.1.1. Thermal runaway fault detection and diagnosis

In this work, we establish a polymerization model and introduce five faults that may cause the thermal runaway phenomenon. The model and datasets are accessible for assessing the performance of MSPM methods in detecting thermal runaway faults during polymerization. We can also diagnose their root causes and severities to avoid potential failures or shutdowns in the system.

6.1.2. Control strategy design

Currently, there are two main PID controllers: the reactor temperature controller and the reactor pressure controller. The reaction rate is typically managed based on empirical knowledge and expertise. Numerous control strategies can be employed to mitigate the possibility of thermal runaway.

6.1.3. Thermal runaway risk analysis

Risk analysis is crucial for industrial processes such as polymerization thermal runaway. By conducting a risk analysis of this benchmark model, we can identify factors contributing to thermal runaway, including reaction heat, monomer concentration, and solvent selection. This enables us to anticipate potential issues and implement appropriate measures to optimize the process and mitigate the risk of thermal runaway.

6.2. Conclusions

In this paper, we present a multivariable, nonlinear mathematical model of a simplified industrial polymerization process. To the best of our knowledge, this is the first publicly available model capable of simulating thermal runaway in polymerization specifically for the development of process monitoring algorithms. The model encompasses five fault scenarios, including excessive initiator addition, the Gel effect, heat transfer fouling, inaccurate thermometer readings, and sticking of the jacket cooling water valve, all of which can lead to thermal runaway. Accompanying the model are relative normal and faulty datasets that are also made publicly available for other researchers to utilize in developing and validating their own process monitoring algorithms. Additionally, we discuss the step-by-step usage procedure of this model and datasets for effective algorithm development. We establish the model's applicability and suitability by testing two types of process monitoring algorithm examples. Furthermore, beyond algorithm development, this model holds potential for applications in control strategy design and thermal runaway risk analysis, thereby contributing to enhanced production process safety and improved product quality.

Declaration of competing interest

The authors declare that they have no known competing financial interests or personal relationships that could have appeared to influence the work reported in this paper.

Acknowledgments

This work was supported in part by the Institute of Zhejiang University-Quzhou, China(IZQ2022KYZX12 and IZQ2022KJ3001), in part by the Zhejiang High-end Chemicals Technology Innovation Center, China(ACTIC-2022-013).

Nomenclature

$[A]_0$	Balanced concentration of A at the gas-liquid interface [mol L^{-1}]
[Y]	Liquid phase concentration of Y [mol L^{-1}]
$\Delta\alpha_M$	Fault parameter
$\Delta\alpha_p$	Fault parameter
ΔH	Standard heat of reaction for chain growth [J mol^{-1}]
ϵ	Model parameter
λ_m	m-th moment of active polymers
μ_m	m-th moment of dead polymers
$\overline{M}_{wcr}$	Weight average molecular weight when $I = t_3$
$\overline{M}_n$	Number average molecular weight
$\overline{M}_w$	Weight average molecular weight
ϕ_M	Fault parameter
ϕ_p	Fault parameter
$\boldsymbol{X}_{mean}$	Sample mean matrix
$\boldsymbol{x}_{mean}$	Sample mean vector
$\boldsymbol{X}_{st}$	Standard deviation matrix
$\boldsymbol{x}_{st}$	Standard deviation vector
$\boldsymbol{x}_{train}$	Training dataset
$\boldsymbol{x}_{test,k}$	test vector
ρ	Latex density [kg m^{-3}]
a	Coefficient
b_1, b_2	Empirical constant
$c_1, c_2, c_3, c_{4.1}, , c_{4.2}c_5$	Fault parameter
$C_{p,A}$	Monomer heat capacity A [J kg^{-1} K^{-1}]
$C_{p,j}$	Jacket media heat capacity [J kg^{-1} K^{-1}]
$C_{p,s}$	Reactor solvent heat capacity [J kg^{-1} K^{-1}]
d	Impeller diameter [m]
E_1	Active energy for initiatir decomposition [J mol^{-1}]
E_2	Active energy for chain initiation [J mol^{-1}]
E_3	Active energy for chain growth [J mol^{-1}]
E_4	Active energy for chain transfer to monomer [J mol^{-1}]
E_5	Active energy for chain transfer to acidic regulator [J mol^{-1}]
E_6	Active energy for chain transfer to chain transfer agent [J mol^{-1}]
E_7	Active energy for chain termination [J mol^{-1}]
F_{gl}	Monomer A dissolution rate in liquid phase [kg s^{-1}]
$F_{in,A}$	Monomer A feed rate [kg s^{-1}]
$F_{in,B}$	Initiator B feed rate [kg s^{-1}]
F_j	Jacket water feed rate [kg s^{-1}]
G	Model parameter
H	Henry's constant for momomer A [Pa L mol^{-1}]
h	Gaussian kernel parameter
I_3	Critical judgementvalue of Gel effect
K	Stirrer constant
k	Mass transfer coefficient related to temperature [kg L mol^{-1} s^{-1}]

k_{10} Pre-exponential factor for initiatir decomposition [s^{-1}]

k_{20} Pre-exponential factor for chain initiation [s^{-1}]

k_{30} Pre-exponential factor for chain growth [s^{-1}]

k_{40} Pre-exponential factor for chain transfer to monomer [s^{-1}]

k_{50} Pre-exponential factor for chain transfer to acidic regulator [s^{-1}]

k_{60} Pre-exponential factor for chain transfer to chain transfer agent [s^{-1}]

$k_{7,\mathrm{real}}$ Actual chain termination rate constant

k_{70} Pre-exponential factor for chain termination [s^{-1}]

m The number of measured variables and manipulated variables

$M_{\mathrm{A,l}}$ Mass of A in liquid phase [kg]

M_{A} Molecular weight of A [$g\,mol^{-1}$]

M_{B} Molecular weight of B [$g\,mol^{-1}$]

M_{j} Mass of jacket media [kg]

M_{s} Mass of reactor solvent [kg]

N Stirrer speed [$r\,s^{-1}$]

N_{FN} The number of false negative samples

N_{FP} The number of false positive samples

N_{TN} The number of true negative samples

N_{TP} The number of true positive samples

$N_{\mathrm{g,A}}$ Amount of A in the gas phase of the reactor [mol]

N_{Y} Amount of Y in the liquid phase of the reactor [mol]

P Gas pressure [Pa]

$Q_{\mathrm{in,j}}$ Heat input to the jacket [J]

Q_{loss} Heat loss to the surroundings [J]

$Q_{\mathrm{out,j}}$ Heat output from the jacket [J]

Q_{r} Reaction heat [J]

Q_{stir} Energy input due to the stirrer [J]

Q_{w} Heat flow through the reactor [J]

Q_{feed} Heat input due to the feeds [J]

R Ideal gas constant [$J\,mol^{-1}\,K^{-1}$]

R_1 Reaction rate of initiator decomposition [$mol\,s^{-1}$]

R_2 Reaction rate of chain initiation [$mol\,s^{-1}$]

R_3 Reaction rate of chain growth [$mol\,s^{-1}$]

R_4 Reaction rate of chain transfer to monomer [$mol\,s^{-1}$]

R_5 Reaction rate of chain transfer to acidic regulator [$mol\,s^{-1}$]

R_6 Reaction rate of chain transfer to chain transfer agent [$mol\,s^{-1}$]

R_7 Reaction rate of chain termination [$mol\,s^{-1}$]

S Heat transfer area [m^2]

T_{gM} Fault parameter

T_{gp} Fault parameter

T_{amb} Temperature of environment [K]

T_{A} Temperature of A feed [K]

$T_{\mathrm{in,j}}$ Temperature of jacket feeds [K]

T_{j} Temperature of jacket media [K]

T_{r} Temperature of reactor [K]

U Heat transfer coefficient [$W\,m^{-2}\,K^{-1}$]

V Total volume of the reactor [m^3]

V_{fcr} Free voolume fraction value when $I = t_3$

V_{f} Free volume fraction

$V_{\mathrm{l,0}}$ Volume of solvent [m^3]

V_{g} Reactor gas volume [m^3]

V_{l} Reactor liquid volume [m^3]

X Monomer conversion

References

Abraham, M.H., Chadha, H.S., Mitchell, R.C., 1995. The factors that influence skin penetration of solutes. J. Pharm. Pharmacol. 47, 8–16.

Allen, J., 2020. Review of polymers in the prevention of thermal runaway in lithium-ion batteries. Energy Rep. 6, 217–224.

Amin, M.T., Khan, F., Ahmed, S., Imtiaz, S., 2021. Risk-based fault detection and diagnosis for nonlinear and non-gaussian process systems using r-vine copula. Process Saf. Environ. 150, 123–136.

Ando, M., Fujita, M., Izato, Y.i., Miyake, A., 2021. A kinetic model for the autocatalytic behavior of nitric acid/formic acid mixtures to predict induction period. Process Saf. Environ. 151, 182–187.

Annaswamy, A.M., Johansson, K.H., Pappas, G., 2024. Control for societal-scale challenges: Road map 2030. IEEE Contr. Syst. Mag. 44, 30–32.

Arunthavanathan, R., Khan, F., Ahmed, S., Imtiaz, S., 2021. A deep learning model for process fault prognosis. Process Saf. Environ. 154, 467–479.

Cai, L., Tian, X., 2014. A new fault detection method for non-gaussian process based on robust independent component analysis. Process Saf. Environ. 92, 645–658.

Cai, P., Deng, X., 2020. Incipient fault detection for nonlinear processes based on dynamic multi-block probability related kernel principal component analysis. ISA T. 105, 210–220.

Chen, H., Jiang, B., Lu, N., 2018. An improved incipient fault detection method based on kullback-leibler divergence. ISA T. 79, 127–136.

Cui, J., Ni, L., Jiang, J., Pan, Y., Wu, H., Chen, Q., 2019. Computational fluid dynamics simulation of thermal runaway reaction of styrene polymerization. Org. Process Res. Dev. 23, 389–396.

Dakkoune, A., Hassimi, L.V., Leveneur, S., Estel, L., Lefebvre, D., 2018. Model-based fault detection and isolation for chemical processes: Application to the prevention of thermal runaway, in: 2018 IEEE Symposium Series on Computational Intelligence (SSCI), IEEE. pp. 1352–1358.

Deng, X., Zhang, X., Liu, X., Cao, Y., 2023. Incipient fault detection of nonlinear chemical processes based on probability-related randomized slow feature analysis. Process Saf. Environ. 169, 797–807.

Dong, J., Jiang, L., Zhang, C., Peng, K., 2022. A novel quality-related incipient fault detection method based on canonical variate analysis and kullback–leibler divergence for large-scale industrial processes. IEEE T. Instrum. Meas. 71, 1–10.

Downs, J.J., Vogel, E.F., 1993. A plant-wide industrial process control problem. Comput. Chem. Eng. 17, 245–255. doi: 10.1016/0098-1354(93)80018-I.

Farina, M., 1987. Chemistry and kinetics of the chain transfer reaction, in: Makromolekulare Chemie. Macromolecular Symposia, Wiley Online Library. pp. 255–272.

Finkler, T.F., Kawohl, M., Piechottka, U., Engell, S., 2014. Realization of online optimizing control in an industrial semi-batch polymerization. J. Process Contr. 24, 399–414.

Gao, S.Z., Wang, J.S., Gao, X.W., 2013. Modeling and advanced control method of pvc polymerization process. J. Process Contr. 23, 664–681.

Han, S., Hua, Y., Lin, Y., Yao, L., Wang, Z., Zheng, Z., Yang, J., Zhao, C., Zheng, C., Gao, X., 2023. Fault diagnosis of regenerative thermal oxidizer system via dynamic uncertain causality graph integrated with early anomaly detection. Process Saf. Environ. 179, 724–734.

Harmouche, J., Delpha, C., Diallo, D., 2014. Incipient fault detection and diagnosis based on kullback–leibler divergence using principal component analysis: Part i. Signal processing 94, 278–287.

Jokilehto, J., 2010. Conservation principles in the international context, in: Conservation. Routledge, pp. 73–83.

Joy, P., Rossow, K., Jung, F., Moritz, H.U., Pauer, W., Mitsos, A., Mhamdi, A., 2019. Model-based control of continuous emulsion co-polymerization in a lab-scale tubular reactor. J. Process Contr. 75, 59–76.

Kano, M., Hasebe, S., Hashimoto, I., Ohno, H., 2002. Statistical process monitoring based on dissimilarity of process data. AIChE Journal 48, 1231–1240.

Learning, L., 2021. The ideal gas law. Fundamentals of Heat, Light & Sound .

Li, S., 2024. A semi-batch polymerization process for fault simulation. URL: https://www.mathworks.com/matlabcentral/fileexchange/169341-a-semi-batch-polymerization-process-for-fault-simulation.

Liu, G., Wilhite, B.A., 2019. Model-based design for inhibition of thermal runaway in free-radical polymerization. Ind. Eng. Chem. Res. 58, 17244–17254.

Liu, G., Wilhite, B.A., 2022. Development of compartment model for inhibition of thermal runaway in free-radical polymerization. Chem. Eng. Sci. 258, 117758.

Liu, N., Hu, M., Wang, J., Ren, Y., Tian, W., 2022. Fault detection and diagnosis using bayesian network model combining mechanism correlation analysis and process data: Application to unmonitored root cause variables type faults. Process Saf. Environ. 164, 15–29.

Marten, F., Hamielec, A., 1982. High-conversion diffusion-controlled polymerization of styrene. i. J. Appl. Polym. Sci. 27, 489–505.

Odgaard, P.F., Stoustrup, J., Kinnaert, M., 2013. Fault-tolerant control of wind turbines: A benchmark model. IEEE T. Contr. Syst. T. 21, 1168–1182.

Pilario, K.E.S., Cao, Y., 2018. Canonical variate dissimilarity analysis for process incipient fault detection. IEEE Trans. on Ind. Informat. 14, 5308–5315.

Pilario, K.E.S., Cao, Y., Shafiee, M., 2019. Mixed kernel canonical variate dissimilarity analysis for incipient fault monitoring in nonlinear dynamic processes. Comput. Chem. Eng. 123, 143–154.

Safaeipour, H., Forouzanfar, M., Casavola, A., 2021. A survey and classification of incipient fault diagnosis approaches. J. Process Contr. 97, 1–16.

Sander, R., 2015. Compilation of henry's law constants (version 4.0) for water as solvent. Atmos. Chem. and Phys. 15, 4399–4981.

Sun, J.G., Cao, Q., et al., 2014. The research on modeling and simulation of tfe polymerization process. Math. Probl. Eng. 2014.

Wang, J., Zhao, C., 2020. A gaussian feature analytics-based dissim method for fine-grained non-gaussian process monitoring. IEEE T. Autom. Sci. Eng. 17, 2175–2181.

Wei, Z., Ji, X., Zhou, L., Dang, Y., Dai, Y., 2022. A novel deep learning model based on target transformer for fault diagnosis of chemical process. Process Saf. Environ. 167, 480–492.

Wu, P., Ferrari, R.M., Liu, Y., Van Wingerden, J.W., 2020. Data-driven incipient fault detection via canonical variate dissimilarity and mixed kernel principal component analysis. IEEE Trans. Ind. Informat. 17, 5380–5390.

Xiao, S., 2019. Kernel canonical variate dissimilarity analysis for fault detection, in: 2019 Chinese Control Conference (CCC), IEEE. pp. 6871–6876.

Yu, J., Yan, X., 2021. A new deep model based on the stacked autoencoder with intensified iterative learning style for industrial fault detection. Process Saf. Environ. 153, 47–59.

Zhao, C., Wang, F., Jia, M., 2007. Dissimilarity analysis based batch process monitoring using moving windows. AIChE journal 53, 1267–1277.

Zhao, C., Wang, F., Mao, Z., Jia, M., Wang, S., 2008. An adaptive dissim algorithm for statistical process monitoring. IFAC Proceedings Volumes 41, 4529–4534.

Zhao, C., Wang, W., Gao, F., 2017. Sparse dissimilarity analysis based on distribution dissimilarity decomposition for online diagnosis of incipient faults, in: 2017 American Control Conference (ACC), IEEE. pp. 5430–5435.

Zhou, J., Zhu, Y., Shao, Z., 2023. A combined passive-active method for diagnosing multiplicative fault. Process Saf. Environ. 178, 959–975.